A Letters Journal Exploring
the Frontiers of Physics

OFFPRINT

Rapid fluid flow and mixing induced in microchannels using surface acoustic waves

M. K. Tan, L. Y. Yeo and J. R. Friend

EPL, **87** (2009) 47003

Please visit the new website
`www.epljournal.org`

TAKE A LOOK AT THE NEW EPL

Europhysics Letters (EPL) has a new online home at

www.epljournal.org

http://www.epljournal.org
epl
A Letters Journal Exploring the Frontiers of Physics
Athens login
Switch to test
IOP login:
Password:
Go
Create account | Alerts | Contact us
Journals Home
Journals List
This Journal
Search
Authors
Referees
Librarians
User Options
Help
This Journal
Partners
Editorial information
Editorial & Advisory Boards
Abstracted in
Request sample copy
For authors
For referees
For co-editors
Pricing & ordering
Events calendar
Copyright & permissions
info@epljournal.org
recommend this journal
e-mail alerts
An easy way to keep up to date
RSS
RSS feed: latest articles
About RSS
EPS
Done

Welcome to the new EPL website

www.epljournal.org is the new online home for *Europhysics Letters* (EPL). This new website features the latest published issues, all articles published since 1996 and journal news, and will be the main contact point for authors, referees and readers of the journal. We are keen to hear your views on the new site, so if you have questions or comments do not hesitate to e-mail us at info@epljournal.org.

Latest issue (complete) No 1, January 2007 (10000-19002)
Open issue No 2, January 2007 (20001-28003)

Current volume
Number 2, January 2007 Go

Journal archive
Vol 77, 2007 Go

Forthcoming articles
An advance list of articles that have been accepted for publication.

This Month's Papers
As a service to authors, all papers published in our journals are free for 30 days from the date of online publication. To make the most of this service sign up for free e-alerts to find out when the latest papers are published in your field.

A truly international journal
Owned by a partnership of 17 European physical societies, EPL is published under the scientific responsibility of the European Physical Society by EDP Sciences, IOP Publishing and Società Italiana di Fisica. We have brought together our expertise to create a high-quality journal for the international scientific community.

Exploring the frontiers of physics
Our vision is for EPL to become a leading home for global physics letters, to offer rapid publication of ground-breaking physics results from the international community, and to provide the broadest coverage of physics research.

ISSN 0295-5075 (Print)
ISSN 1286-4854 (Online)

2005 IMPACT FACTOR
2.237

Take a look for the latest journal news and information on:

- reading the latest articles, free!
- receiving free e-mail alerts
- submitting your work to EPL

www.epljournal.org

A Letters Journal Exploring
the Frontiers of Physics

August 2009

EPL, **87** (2009) 47003
doi: `10.1209/0295-5075/87/47003`

`www.epljournal.org`

Rapid fluid flow and mixing induced in microchannels using surface acoustic waves

M. K. Tan, L. Y. Yeo and J. R. Friend[(a)]

*Micro/Nanophysics Research Laboratory, Department of Mechanical Engineering, Monash University
Melbourne, Victoria 3800 Australia*

received 26 March 2009; accepted in final form 29 July 2009
published online 4 September 2009

PACS `77.65.Dq` – Acoustoelectric effects and surface acoustic waves (SAW) in piezoelectrics
PACS `47.61.-k` – Micro- and nano- scale flow phenomena
PACS `43.25.+y` – Nonlinear acoustics

Abstract – Very-high-frequency surface acoustic waves, generated and transmitted along single-crystal lithium niobate, are used to drive homogeneous aqueous suspensions of polystyrene nanoparticles along microchannels. At a few hundred milliwatts, uniform and mixing flows with speeds of up to 10 mm/s were obtained in centimetres-long rectangular channels with cross-sectional dimensions of tens to a few hundreds of microns. A transition from uniform to mixing flow occurs as the channel width grows beyond the wavelength of sound in the fluid at the chosen excitation frequency. At far lower input powers, the suspension agglomerates into equally spaced, serpentine lines coincident with nodal lines in the acoustic pressure field. We expose the physics underlying these disparate phenomena with experimental results aided by numerical models.

Copyright © EPLA, 2009

Introduction. – The dominance of surface tension and viscous forces at small scales enormously complicates efficient transport and mixing in microfluidic technologies. In searching for solutions to this problem, we describe and explain three physical aspects peculiar to very-high-frequency (VHF) surface acoustic wave (SAW) excitation of fluids in a microchannel: an ability to drive fluids along the channel at 1–10 mm/s [1], the appearance of vortices and concomitant mixing under specific conditions, and the collection and transport of particle suspensions. The first two phenomena offer —by merely changing the SAW frequency— controlled switching between uniform flow for fluid delivery and vortex-laden flows for mixing in the same microchannel, eliminating the complex architectures [2] required to induce mixing. In a similar vein, the manipulation of particle-laden flows is directly applicable to sorting or patterning.

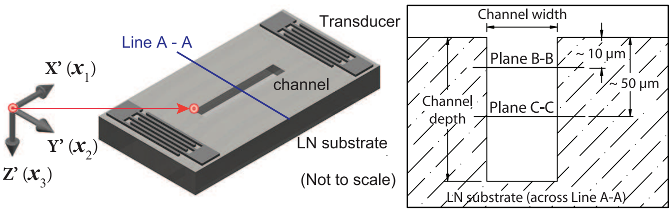

Fig. 1: (Color online) The cut channel, indicating the different planes used to obtain experimental images. The dot at the corner of the channel indicates the origin of the coordinates: x_1, x_2, and, x_3 point along the channel's length $\mathcal{L}_{\mathrm{ch}}$, width $\mathcal{W}_{\mathrm{ch}}$, and into the substrate along the channel's depth $\mathcal{D}_{\mathrm{ch}}$, respectively.

The SAW is a *Rayleigh* wave [3] generated by a sinusoidal electric potential applied to an interdigital transducer (IDT) on the surface of a 127.68° y–x cut, x-propagating lithium niobate (LN) single-crystal piezoelectric substrate (fig. 1) formed using standard UV photolithography. While the SAW is confined in its propagation from the transducer along the anisotropic substrate's x-axis at a velocity $v_{\mathrm{SAW}} \approx 3990\,\mathrm{m/s}$, contact with a fluid medium atop the substrate causes some of the SAW's energy to be radiated into the fluid. With sufficient intensity, this acoustic energy propagates as finite amplitude sound radiation traveling at a speed $c_0 < v_{\mathrm{SAW}}$ ($c_0 \approx 1450\,\mathrm{m/s}$ in water at room temperature) in a direction defined by the *Rayleigh angle* $\theta_{\mathrm{SAW}} = \sin^{-1}(c_0/v_{\mathrm{SAW}})$. This forms an (*Eckart* [4]) *acoustic streaming* force in the fluid due to the nonzero and temporally phase-shifted distribution of the pressure and velocity [5] over centimetre-order length scales. *Boundary layer streaming* [5] may also arise due to the

---

[(a)] E-mail: `james.friend@eng.monash.edu.au` transmission of shear from the substrate to the fluid and —in contrast to Eckart streaming— is confined to a thin viscous boundary layer of thickness $\delta_v \equiv \sqrt{2\mu/\rho_f\omega}$ [6], where μ and ρ_f are the fluid viscosity and density, respectively, and ω is the angular frequency. Though this form of streaming exists only in the boundary layer, its effects extend outside the layer, driving motion in the bulk of the fluid [7] as *Stokes drift* [8]. For particles suspended in such fluids, one must consider the combined effect of Stokesian drag forces (F_{drag}) from the adjacent fluid driven by acoustic streaming and the direct acoustic forces (F_{rad}) on the particles themselves [9].

The acoustic radiation force F_{rad} on an isolated small rigid spherical particle ($R_p \ll \lambda_f$) in a standing-wave acoustic radiation field in an ideal fluid may be approximated as $F_{\text{rad}} \sim \rho_f(\omega/c_0)R_p^3|u_1|^2 \sin(2\omega x/c_0)\mathcal{F}(\rho_f/\rho_p)$ [10,11], where R_p is the radius of the particle, ρ_p is the density of the particle, x is the distance, and u_1 is the acoustic particle velocity in the fluid, essentially the velocity fluctuation produced by the passage of the wave. The relative density factor is $\mathcal{F}(\rho_f/\rho_p) = \left(1 + \frac{2}{3}(1-\rho_f/\rho_p)\right) / \left(2 + \rho_f/\rho_p\right) = 0.328$ [10] for $\rho_f = 1000\,\text{kg/m}^3$ and $\rho_p = 1050\,\text{kg/m}^3$ for water and polystyrene, respectively, used throughout this study. In stationary waves, the particles with $\rho_p > \rho_f$ must move to the velocity antinodes at $x = \pm\frac{1}{2}\pi c_0/\omega, \pm\frac{3}{2}\pi c_0/\omega \ldots$. With the nonlinear velocity correction (acoustic streaming velocity u_{dc}), the particle is subjected to a drag force, $F_{\text{drag}} \sim \mu\pi R_p u_{\text{dc}}$ [11,12], due to the net motion of the fluid. The suspended particles therefore follow the streamlines when $F_{\text{drag}} \gtrsim F_{\text{rad}}$ is satisfied. Note that particle compressibility and second-order acoustic wave forces due to scattering from nearby particles are insignificant in the regime under study here, as described by Doinikov's work [13].

The interaction of SAW with sessile droplets has been explored [14], thoroughly analysed, and exploited for droplet transport [15], chaotic convection [16], microparticle concentration [17], and atomisation [18,19]. Curiously, the same interaction in microchannels remains unexplored, where the potential number of applications is arguably far greater due to the ubiquity of such channels in microfluidics. Here we examine SAW-fluid interactions in such channels, combining experimental observations and numerical modelling to explain the diverse phenomena.

Channel flow induced by SAW. – We cut rectangular microchannels $\mathcal{L}_{\text{ch}} = 10\,\text{mm}$ long and $\mathcal{D}_{\text{ch}} = 180\,\mu\text{m}$ deep with widths of $\mathcal{W}_{\text{ch}} = 30$, 50, 150, 200 and 280 μm into the LN substrates of devices designed to operate in the VHF range at 20 and 30 MHz using a KrF 248 nm exciplex laser (Extech Ltd., Oxford, England) as shown in fig. 1. The SAW wavelength λ_{SAW} is approximately 200 μm and 133 μm, respectively. The microchannel was then filled with a deionized aqueous, homogeneous suspension of either $\phi_p = 500\,\text{nm}$ or 1 μm diameter spherical fluorescent polystyrene particles (BioScientific, Gymea NSW) both selected to ensure that $\phi_p \ll \lambda_f$ and $\phi_p \ll \mathcal{W}_{\text{ch}}$: at room temperature, $\lambda_f \approx 73$ and 48 μm for the 20 MHz and 30 MHz sound waves in water, respectively. The different planes in fig. 1 are sections along the channel where experimental observations were made. A damping material (α-gel, Geltec Ltd., Yokohama, Japan) was used to minimize wave reflection from the ends of the substrate and thus suppress wave interference throughout. The flow behaviour in the channel was determined using microscopic flow visualization (BXFM stereomicroscope and iSpeed camera, Olympus, Japan) at 60 frames/second.

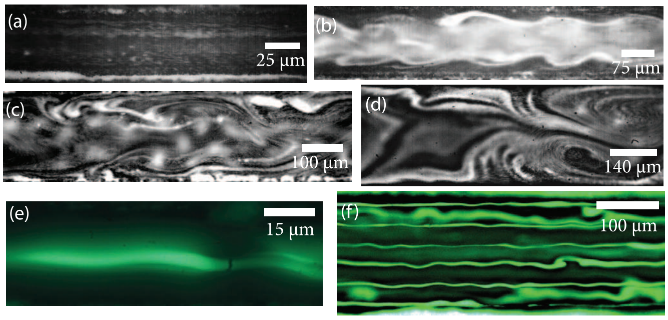

Fig. 2: (Color online) Images (a)–(d) showing typical flow behavior along plane B-B in $\mathcal{W}_{\text{ch}} = 50$, 150, 200, and 280 μm wide microchannels while driven by 20 MHz SAW. Note the transition from (a) uniform flow to (d) mixing flow as the width of the channel is increased while the frequency and input power are held constant at 20 MHz and 400 mW, respectively. The behavior along plane C-C is rather different: 500 nm particles collect into either one or six lines in a (e) 30 μm or (f) 200 μm wide channel, respectively, under 30 MHz SAW excitation.

In a 50 μm wide channel, the fluid uniformly flows in the same direction as the SAW radiation at approximately 3.5 mm/s along plane B-B (fig. 2(a)) while the SAW device is driven at 20 MHz and 400 mW (see supplementary video `effectofchannelwidth_1.mov`). As the width of the channel in the 20 MHz device is increased from $\mathcal{W}_{\text{ch}} = 150$, 200, to 280 μm, the flow becomes progressively irregular in figs. 2(b)–(d) while holding the input power constant at 400 mW. Similarly, the uniform flow transitions through oscillatory to vortex-rich, mixing flow in the 30 MHz device when $\mathcal{W}_{\text{ch}}$ increases beyond 30 μm. In both cases flow irregularities appear when $\mathcal{W}_{\text{ch}} > \lambda_f$, indicating a frequency-dependent transition between uniform and mixing flow that presents interesting possibilities for mixing through using higher harmonics or a second interdigital electrode in a SAW device. At plane C-C and deeper in the channel, however, the streaming flow velocity is lower and particles are therefore able to collect along equally spaced lines roughly parallel to the x-axis as shown in figs. 2(e), (f).

Numerical model. – To analyse the problem, a two-dimensional numerical model of the phenomena was constructed for the (x_1, x_2)-plane illustrated in figs. 1 and 3, including the linear piezoelectric coupling equations [20] and hydrodynamic equations [5,6,21].

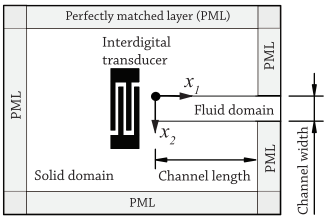

Fig. 3: The computation domains in the numerical model; the solid domain is bounded by a PML to minimize wave reflections.

Governing equations for the solid. The time-domain piezoelectric constitutive relations combined with the dynamic equations are given by (summation over repeated subscripts assumed throughout) [20,22]

$$\frac{\partial D_i}{\partial t} = e_{ikl}\frac{\partial S_{kl}}{\partial t} + \epsilon^{\mathrm{S}}_{ik}\frac{\partial E_k}{\partial t}, \tag{1}$$

$$\frac{\partial T_{ij}}{\partial t} = c^{\mathrm{E}}_{ijkl}\frac{\partial S_{kl}}{\partial t} - e_{kij}\frac{\partial E_k}{\partial t}, \qquad \text{and} \tag{2}$$

$$\rho_{\mathrm{s}}\frac{\partial v_j}{\partial t} = \frac{\partial T_{ij}}{\partial x_i}, \tag{3}$$

where D_i represent the electric displacement components, e_{ikl} are the piezoelectric stress (third rank) tensor components, S_{kl} are the mechanical strain (second rank) tensor components, $\epsilon^{\mathrm{S}}_{ik}$ are the dielectric constant (second rank) tensor components at constant strain, E_k the electric field, T_{ij} represent the stress (second rank) tensor components, c^{E}_{ijkl} the elastic stiffness (fourth rank) tensor components at constant electric field, ρ_{s} the density, and v_j are the velocity components, with $i,j,k,l \in \{1,2,3\}$ corresponding to the orthogonal Cartesian axes x_1, x_2, x_3. To solve eqs. (1)–(3), we invoke the quasi-static approximation $\partial \mathbf{D}/\partial t = \nabla \times \mathbf{H} \approx 0$, where $\mathbf{H}$ is the magnetic field vector. To complete the description of the basic behavior of acoustic waves in a piezoelectric solid, we use the infinitesimal strain-displacement relationship $\partial S_{kl}/\partial t = \frac{1}{2}[(\partial^2\xi_k/\partial x_l \partial t) + (\partial^2 \xi_l/\partial x_k \partial t)]$ where ξ_k is the particle displacement [20]. Material properties —e_{ikl}, $\epsilon^{\mathrm{S}}_{ik}$ and c^{E}_{ijkl}— need to be transformed to the correct orientation. We use the bond transformation principle [20] to transform these material constants from the crystal's principal axes to the 128-YX cut configuration. Equations (1)–(3), are solved using a finite-difference time-domain (FDTD) method [22]. For a 2D model (fig. 3), propagation in the x_3-direction is assumed to be zero, thus $\partial/\partial x_3 = 0$. A split-field perfectly matched layer (PML) boundary condition is employed to minimize wave reflection from the boundaries [23]. The wave amplitude decays quadratically when incident on the PML with a loss function represented by $\sigma_i = \sigma_{\max}[(x_i - x_0)/\delta_{\mathrm{PML}}]^2$ [23], where $(x_i - x_0)$ indicates the location of the nodes within the PML layer, δ_{PML} is the thickness of the PML, and $\sigma_{\max}$ is a numerical constant. A sinusoidal electric potential, $\phi = \phi_{\text{p-p}} \sin(2\pi x_i/\lambda_{\mathrm{SAW}})\sin(\omega t)$, is applied on the surface of the solid to launch the surface wave.

Governing equations for the fluid. In the fluid medium, the equations describing mass and momentum conservation, and equation of state [5,6,12,21] are as follows:

$$\frac{\partial \rho_{\mathrm{f}}}{\partial t} + \boldsymbol{\nabla}\cdot(\rho_{\mathrm{f}}\mathbf{u}) = 0, \tag{4}$$

$$\rho_{\mathrm{f}}\frac{\partial \mathbf{u}}{\partial t} + \rho_{\mathrm{f}}(\mathbf{u}\cdot\boldsymbol{\nabla})\,\mathbf{u} = -\boldsymbol{\nabla}p + \mu\boldsymbol{\nabla}^2\mathbf{u} + \left(\mu_{\mathrm{B}} + \frac{\mu}{3}\right)\boldsymbol{\nabla}\boldsymbol{\nabla}\cdot\mathbf{u}, \tag{5}$$

$$\text{and} \quad p - p_0 = c_0^2(\rho_{\mathrm{f}} - \rho_{\mathrm{f0}}) + \frac{1}{2}\left(\frac{\partial c^2}{\partial \rho_{\mathrm{f}}}\right)_s (\rho_{\mathrm{f}} - \rho_{\mathrm{f0}})^2, \tag{6}$$

where μ_{B} is bulk viscosity, p is the pressure, $\mathbf{u}$ is the fluid velocity, and s is the entropy. The subscript "0" refers to the quantities at equilibrium. The governing equations given by eqs. (4)–(6) are then decomposed through a perturbation expansion of each of the dependent variables about a small parameter $\varepsilon = \mathcal{U}/c_0$, where $\mathcal{U}$ is the characteristic acoustic particle velocity, to the fluid velocity, pressure and density field of the form [5,6,21] $\mathbf{u} = \mathbf{u}_0 + \varepsilon\mathbf{u}_1 + \varepsilon^2\mathbf{u}_2 + \mathcal{O}(\varepsilon^3)$, $p = p_0 + \varepsilon p_1 + \varepsilon^2 p_2 + \mathcal{O}(\varepsilon^3)$, and $\rho_{\mathrm{f}} = \rho_{\mathrm{f0}} + \varepsilon\rho_{\mathrm{f1}} + \varepsilon^2\rho_{\mathrm{f2}} + \mathcal{O}(\varepsilon^3)$. The subscripts "1" and "2" refer to the first-order and second-order approximations, respectively. At equilibrium, $\mathbf{u}_0 = 0$, $p_0 \approx 10^5$ Pa, and $\rho_{\mathrm{f0}} \approx 998\,\mathrm{kg/m^3}$ for water at room temperature. By substituting these expansions into eqs. (4)–(6), we obtain first-order equations describing the propagation of acoustic waves in the fluid and second-order equations describing acoustic streaming.

First-order sound field. The first-order approximations to eqs. (4)–(6) are [5,6,21]

$$\frac{\partial \rho_{\mathrm{f1}}}{\partial t} + \rho_{\mathrm{f0}}(\boldsymbol{\nabla}\cdot\mathbf{u}_1) = 0, \tag{7}$$

$$\rho_{\mathrm{f0}}\frac{\partial \mathbf{u}_1}{\partial t} = -\boldsymbol{\nabla}p_1 + \mu\boldsymbol{\nabla}^2\mathbf{u}_1 + \left(\mu_{\mathrm{B}} + \frac{\mu}{3}\right)\boldsymbol{\nabla}\boldsymbol{\nabla}\cdot\mathbf{u}_1, \tag{8}$$

$$\text{and} \qquad p_1 = c_0^2\rho_1, \tag{9}$$

respectively. The FDTD method is also used to solve eqs. (7)–(9) [24]. In our numerical model, the distance between nodes in the discretisation is larger than the viscous boundary layer thickness δ_v. In order to resolve this missing viscous dissipation in the boundary layer due to the numerical discretisation, eq. (7) is decomposed into an irrotational longitudinal-velocity $\mathbf{u}_l$ component that satisfies $\nabla \times \mathbf{u}_l = 0$ [6], $\rho_{\mathrm{f0}}(\partial \mathbf{u}_l/\partial t) = -\nabla p_1 + (\mu_B + \frac{4}{3}\mu)$ $\nabla\nabla\cdot\mathbf{u}_l$, capturing the propagation of sound in the bulk of the fluid, and a transverse velocity $\mathbf{u}_t$ component that satisfies $\nabla\cdot\mathbf{u}_t = 0$ [6]: $\rho_{\mathrm{f0}}(\partial\mathbf{u}_t/\partial t) = -\mu\nabla\times\nabla\times\mathbf{u}_t$, and describes the behavior of sound in the boundary layer $x \leqslant \delta_v$. An analytical solution is used to approximate the transverse velocities at the nodes located directly above the solid-fluid boundary [6]: $u_{tx1} \approx A_{x1}\exp\{ik_t x_1 + (y/\delta_v)(i-1) - i\omega t\}$ and $u_{tx2} \approx A_{x2}k_t\delta_v$ $(1-i)\exp\{ik_t x_1 + (y/\delta_v)(i-1) - i\omega t\}/2$, where A_{x1} and A_{x2} are the velocity amplitudes on the solid surface in the x_1- and x_2-direction, respectively; y is the distance from the solid-fluid boundary, and $k_t \approx \omega / c_0$. At the solid-fluid interface, continuity between the substrate and fluid velocities is maintained using linear interpolation between the meshes while preserving the interface profile. Since the equations for the solid and fluid are solved simultaneously, at each time step the fluid pressure is coupled back into the solid through conservation of force at the interface; $\sum_{i=1}^{i=n_\mathrm{f}} p_1 = \sum_{i=1}^{i=n_\mathrm{s}} T_2$ at $x_2 = 0$ and $\mathcal{W}_\mathrm{ch}$, where n_s and n_f are the total number of nodes for the solid and fluid at the interface.

Second-order fluid streaming. In the second-order system, the fluid motion consists of a superposition of the steady-state and the time-oscillating harmonic flows. Substituting expanded variables into eqs. (4) and (5), collecting terms of second-order, and subsequently time averaging ($\langle a \rangle = 1/T \int_0^T a(t)\,\mathrm{d}t$) all second-order terms, the following equations are obtained [5,21]:

$$\mathbf{F}_\mathrm{dc} \equiv \rho_\mathrm{f0} \frac{\mathbf{u}_\mathrm{dc}}{\partial t} + \boldsymbol{\nabla} p_\mathrm{dc} - \mu \boldsymbol{\nabla}^2 \mathbf{u}_\mathrm{dc} - \left(\mu_\mathrm{B} + \frac{\mu}{3} \right) \boldsymbol{\nabla} \boldsymbol{\nabla} \cdot \mathbf{u}_\mathrm{dc}, \tag{10}$$

where the body force density $\mathbf{F}_\mathrm{dc}$ (N/m^2) is given by

$$\mathbf{F}_\mathrm{dc} = - \left\langle \rho_\mathrm{f1} \frac{\partial \mathbf{u}_1}{\partial t} \right\rangle - \rho_\mathrm{f0} \langle (\mathbf{u}_1 \cdot \boldsymbol{\nabla}) \, \mathbf{u}_1 \rangle, \tag{11}$$

wherein the parenthesis $\langle \cdot \rangle$ refers to time averaging and the subscript "dc" refers to the steady state. The first-order fluid velocity $\mathbf{u}_1$ is then substituted into eq. (11) to obtain the body force distribution, while the streaming velocity $\mathbf{u}_\mathrm{dc}$, is obtained by solving eq. (10) using the conventional finite-difference approach [25]. Through the method of perturbation expansions, the quantities of the expanded variables in the second-order system are much smaller than their first-order counterparts, *i.e.*, $\mathbf{u}_\mathrm{dc} \ll \mathbf{u}_1$ and $p_\mathrm{dc} \ll p_1$, therefore the second-order system is not coupled with the solid.

Our numerical model described above is considerably more detailed than has been considered in the past [26], capturing fluid-structural coupling, including the effects of oscillating boundary conditions with temporally varying phase as required with Rayleigh waves, viscosity and the concomitant formation of a viscous boundary layer, and the attenuation of the SAW as it propagates along the channel due to the presence of the fluid within. That said, the numerical analysis does not directly include the particles used in the experimental work to characterise the flow. Doing so would greatly complicate the analysis for little benefit, since the particle density in the experiments is purposely kept low to avoid affecting the fluid's behaviour, *i.e.*, to keep it newtonian, and to allow us to see what is happening without being overwhelmed with an excessive number of particles. We do consider, however, how the particles that are present are affected by the fluid flow and acoustic field in the following part of the paper.

Underlying physical mechanisms. – We now turn our attention to understanding the physical mechanisms responsible for three interesting characteristics of the flow and particle behavior in the microchannel: particle collection in serpentine lines parallel to the channel walls, transition between uniform and vortical flow, and particle motion opposing the SAW propagation. Results from the numerical model are provided in fig. 4 onward. The qualitative agreement between analysis and experiment provides coherent insight into the counterintuitive physical phenomena. The computed magnitude of the sound velocity $|\mathbf{u}_1|$ is shown in fig. 4 after 4 and 10 cycles of 20 MHz signal input in a 280 μm wide channel. We observe the emergence of a transverse standing acoustic wave at a distance approximately 560 μm ($2 \times \mathcal{W}_\mathrm{ch}$) downstream from the leading edge of the channel ($x_1 = 0$), outside the domain influenced by direct SAW irradiation from the channel end at left. Given that the two side walls of the microchannel at $x_2 = 0, \mathcal{W}_\mathrm{ch}$ act as parallel radiators, the transmitted acoustic waves superimpose to form a transverse standing-wave across the channel width. It is this standing wave that appears to cause agglomeration of particles along lines parallel to the walls of the channel.

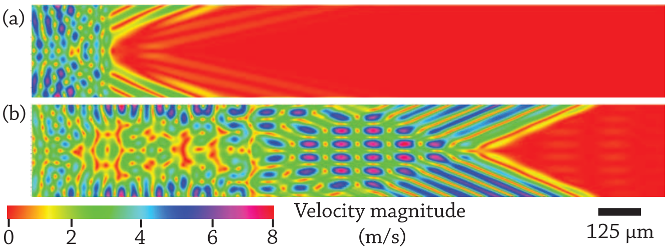

Fig. 4: (Color online) The channel's fluid velocity magnitude, viewed top-down, with x_1 from left to right. Over time —(a) 4 and (b) 10 cycles of 20 MHz signal input, respectively— the SAW refracts into the channel. At far left, the SAW is directly transmitted into the fluid from the solid at the end of the channel, while slightly farther to the right, the radiation from the end of the channel interferes with the radiation being emitted from the channel sides at the Rayleigh angle. Farther to the right, especially at the center in (b), the acoustic radiation from the channel's sides dominate because the SAW is far faster in the solid than the fluid, outrunning the radiation propagating in the fluid along the channel in the x_1-direction.

Numerical and experimental results in fig. 5 indicate 500 nm particles are trapped at the nodes of the pressure field. A 280 μm wide channel under 20 MHz SAW excitation forms six lines of particles aligned to the quiescent regions in the pressure field in the fluid. This is consistent with past results [10–12] since the density of the particles ($\rho_\mathrm{p} \approx 1050\,\mathrm{kg/m^3}$) is slightly higher than the density of the fluid, *i.e.*, $\rho_\mathrm{p} > \rho_\mathrm{f}$. Figure 5(a) shows the solution corresponding to fig. 4(b) for the first-order fluid pressure field, p_1, in the 280 μm wide channel at the end of the tenth cycle. Also shown are 500 nm particles as they collect along lines in plane C-C (fig. 5(b)); the separation between the particle collection lines is approximately 36 μm for the 20 MHz device and 24 μm for a 30 MHz device (not shown), corresponding to $\lambda_\mathrm{f}/2$ for both the computation

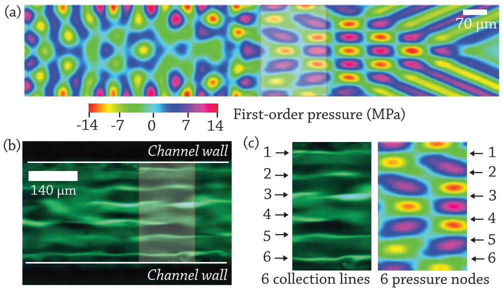

Fig. 5: (Color online) Calculated (a) first-order pressure distribution, p_1, in the fluid in a 280 μm wide channel shows the standing wave formed by cross-channel interference between waves propagating from either side of the channel after 10 cycles. Experimental image (b) shows the collection of 500 nm particles at matching locations across the 280 μm channel along plane C-C when driven by 20 MHz SAW. Comparison (c) between the numerical and experimental results indicate that the particles collect along the nodes of the pressure field.

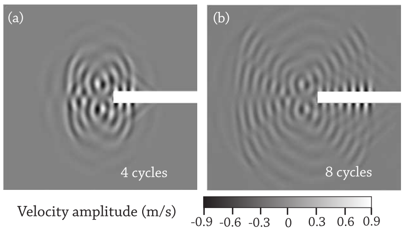

Fig. 6: Velocity contour plots (a) and (b) of v_2 for 4 and 8 cycles, respectively, of waves propagating in the 128-YX LN when a sinusoidal electric potential is applied on one interdigital transducer electrode pair (see fig. 1); the fluid-filled channel is represented by the white slot at the right of each image. The motions of the solid elements (v_2) along the side walls at $x_2 = 0, \mathcal{W}_{\rm ch}$ are 180° out of phase.

and experiment. The number of collection lines is always an integer number of nodal lines with separation $\lambda_{\rm f}/2$ that fit within the given channel width, consistent with past studies [27,28] and our results in fig. 2(e), (f). The different number of collection lines in these results is due to the different channel widths. Similar behavior is observed if 1 μm particles are used.

The motion of the solid elements v_2 along the side walls at $x_2 = 0, \mathcal{W}_{\rm ch}$ as shown in fig. 6, are 180° out of phase. As the sound waves emanate from these side walls, they form an interference pattern in the fluid, shown clearly in figs. 4 and 5. Therefore, asymmetry in the instantaneous transverse velocity, v_2, of the standing wave may occur only if $\mathcal{W}_{\rm ch} > \lambda_{\rm f}$ and $\mathcal{W}_{\rm ch} \neq n\lambda_{\rm f}$ where $n = 1, 2, \ldots$. Since the transition from uniform flow in fig. 2(a) to the oscillatory behavior exhibited in figs. 2(b)–(d) can be attributed to symmetry breaking of the instantaneous transverse velocity field, it then becomes clear why the transition is observed when $\mathcal{W}_{\rm ch} > \lambda_{\rm f}$.

These particles counterintuitively move along the lines in a direction *opposing* the propagation direction of the SAW (figs. 7(a)–(d)), though in agreement with the numerically obtained velocity field shown in fig. 7(e).

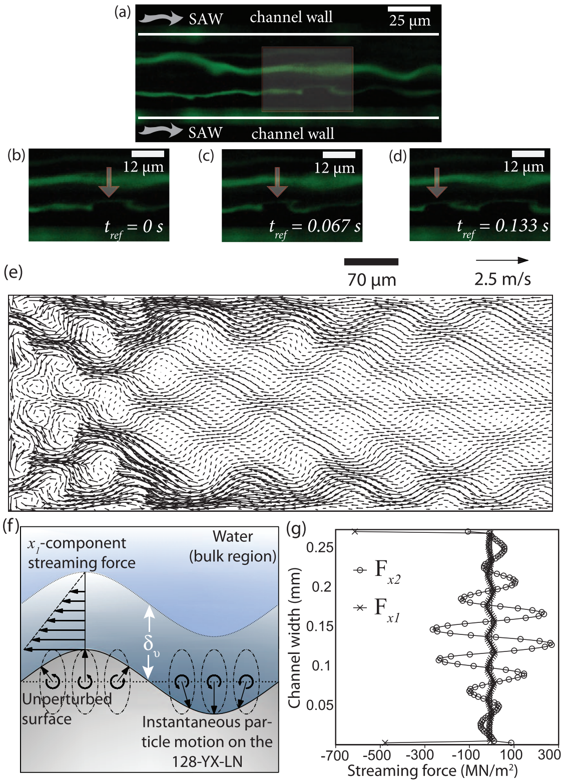

Fig. 7: (Color online) The (a) accumulation of 500 nm particles at the nodes of the pressure field in a 150 μm wide channel appear to be moving right to left along the nodal lines in opposition to the SAW propagating from left to right, as shown in the magnified sequence (b), (c), (d). A computed vector plot (e) of the acoustic streaming velocity after 12 cycles of signal input indicates the flow in the 280 μm wide channel *opposes* the SAW propagation. The reason for the serpentine deformation of the nodal lines is (f) illustrated to be a consequence of the channel wall motion and the vortical flow in the viscous boundary layer of thickness δ_v, giving rise to transverse streaming forces (g) calculated in the x_1 (°) and x_2 (×) directions at $x_1 = 1.48$ mm.

Figure 7(f) depicts the trajectories of the elements in the solid wall adjacent to the fluid at $x_2 = 0, \mathcal{W}_{\rm ch}$; note the *retrograde* trajectory of the wall to the direction of SAW propagation [5]. The large acceleration of these elements gives rise to a large streaming force in the x_1-direction within the viscous boundary layer of thickness $\delta_v \approx 4.9 \times 10^{-7}$ m due to the large dissipative effects there. Note the sharp increase in F_{x_1} near the wall in fig. 7(g). Consequently, strong clockwise vortical flow arises in the boundary layer in fig. 7(f). Outside the boundary layer, the effects of fluid compression become insignificant, and a net fluid flow develops in opposition to the direction of the SAW radiation [5]. The clockwise vortices generate a time-averaged inertial force in the bulk of the fluid. This can be shown by recasting eq. (11) in terms of the vorticity $\mathbf{\Omega} = \frac{1}{2}\nabla \times \mathbf{u}_1$:

$$\mathbf{F}_{\rm dc} = -\frac{1}{c_0^2}\left\langle p_1 \frac{\partial \mathbf{u}_1}{\partial t}\right\rangle - \frac{\rho_0}{2}\langle \nabla\left(\mathbf{u}_1\cdot\mathbf{u}_1\right)\rangle + 2\rho_0\langle \mathbf{u}_1 \times \mathbf{\Omega}\rangle. \tag{12}$$

The last term on the right-hand side of the equation above resembles the effective slip [5] or Stokes' drift [8] boundary condition at $x_2 = \delta_v, \mathcal{W}_{\rm ch} - \delta_v$, and gives rise to flow in the bulk opposing the propagation direction of the SAW across the entire width of the channel (fig. 7(e)). This is predicted by the small but net negative values of F_{x_1} in fig. 7(g) averaged across the channel cross-section, and is further consistent with the experimentally observed direction in which the particles move (figs. 7(b)–(d)).

A closer experimental examination of the particle "lines" exposes serpentine-like undulations of particle trajectories in figs. 7(b)–(d). This is consistent with the local variation of the numerically predicted transverse velocity along x_2, illustrated in fig. 7(e). The undulation of the channel walls as a consequence of the SAW radiation, depicted in fig. 7(f), generates a streaming force in the transverse direction F_{x_2}. It is much stronger in this direction than in the axial direction F_{x_1} in fig. 7(f), suggesting why the serpentine-like particle trajectories in figs. 7(b)–(d) appear. Essentially, these suspended particles in aqueous solution are subjected to two dominant forces: $F_{\rm rad}$ and $F_{\rm drag}$. The particles are driven by the first-order standing wave field to accumulate at nodal lines of the pressure field and drawn along the lines by the acoustic streaming in opposition to the propagation direction of the SAW. By using the quantities $R_{\rm p} \approx 5 \times 10^{-7}$ m, $f \approx 20 \times 10^6$ Hz, and $\mu \approx 0.789 \times 10^{-3}$ kg/(m·s), we find $F_{\rm rad} \sim 10^{-11} u_1^2$ and $F_{\rm drag} \sim 10^{-9} u_{\rm dc}$. We measured $u_1 \sim 10^{-1}$ m/s on the surface of the solid substrate using laser Doppler vibrometry (Polytec MSA-400, Waldbrunn, Germany) and determined the streaming fluid flow speed for the plane C-C (*see* fig. 1) to be $u_{\rm dc} \sim 10^{-4}$ m/s by high-speed microvideography, giving $F_{\rm drag} \sim 10^{-13}$ N while $F_{\rm rad} \sim 10^{-13}$ N, suggesting the particles trapped along the pressure node lines will tend to stay, though they do experience a drag force $F_{\rm drag}$ as a result of the acoustic streaming responsible for their motion along these lines. Along plane B-B, on the other hand, the fluid flow is faster; we measured $u_{\rm dc} \sim 10^{-3}$ m/s, giving $F_{\rm drag} \sim 10^{-12}$ N, greater than $F_{\rm rad} \sim 10^{-13}$ N. The acoustic streaming overwhelms the acoustic radiation forces on the particles, dragging the particles out of the nodal lines and into the vortex mixing flow seen in fig. 2(b)–(d).

With these features, the two-dimensional model offers sufficient veracity to describe the behavior of the experimentally observed flow even with a free surface along the top of the fluid channel absent in the numerical treatment. Capillary waves that may appear as a consequence of VHF SAW excitation and which are so vital to other configurations for atomisation [18] or droplet motion [29] are weak here. We speculate the undulating flow patterns appearing in channels of widths larger than the wavelength of sound, $\mathcal{W}_{\rm ch} > \lambda_{\rm f}$, in fig. 2(b)–(d) arise from the same vortical streaming patterns observed in fig. 7(e), since the configuration and characteristic length scales of these patterns, 50–100 μm, are similar in both the experiments and numerical results. The reversal in the net flow direction in plane B-B occurs due to flow conservation which requires the fluid to recirculate within the closed microchannel, perhaps extending to closed microchannel pumps [30].

REFERENCES

[1] Laser D. and Santiago J., *J. Micromech. Microeng.*, **14** (2004) R35.

[2] Stone H., Stroock A. and Ajdari A., *Annu. Rev. Fluid Mech.*, **36** (2004) 381.

[3] White R. and Voltmer F., *Appl. Phys. Lett.*, **7** (1965) 314.

[4] Eckart C., *Phys. Rev.*, **73** (1948) 68.

[5] Bradley C., *J. Acoust. Soc. Am.*, **100** (1996) 1399.

[6] Morse P. and Ingard K., *Theoretical Acoustics* (MacGraw-Hill) 1968.

[7] Riley N., *Annu. Rev. Fluid Mech.*, **33** (2001) 43.

[8] Bertelsen A., Svardal A. and Tjøtta S., *J. Fluid Mech.*, **59** (1973) 493.

[9] Aboobaker N., Blackmore D. and Meegoda J., *Appl. Math. Model.*, **29** (2005) 515.

[10] King L., *Proc. R. Soc. London, Math. Phys. Sci.*, **861** (1934) 212.

[11] Qi Q. and Brereton G., *IEEE Trans. Ultrason. Ferroelectr. Freq. Control*, **42** (1995) 619.

[12] Rozenberg L., *High-Intensity Ultrasonic Fields* (Plenum Press) 1971.

[13] Doinikov A., *Phys. Rev. E*, **54(6)** (1996) 6297.

[14] Yeo L. and Friend J., *Biomicrofluidics*, **3** (2009) 012002.

[15] Tan M., Friend J. and Yeo L., *Lab Chip*, **7** (2007) 618.

[16] Frommelt T., Kostur M., Schäfer M., Talkner P., Hänggi P. and Wixforth A., *Phys. Rev. Lett.*, **100** (2008) 034502.

[17] Li H., Friend J. and Yeo L., *Biomed. Microdevices*, **9** (2007) 647.

[18] Qi A., Yeo L. and Friend J., *Phys. Fluids*, **20** (2008) 074103.

[19] Friend J., Yeo L., Arifin D. and Mechler A., *Nanotechnology*, **19** (2008) 145301.

[20] Auld B., *Acoustic Fields and Waves in Solids* (Wiley) 1973.

[21] Nyborg W., *Acoustic Streaming* (Academic Press) 1965.

[22] Chagla F. and Smith P., *IEEE Trans. Ultrason. Ferroelectr. Freq. Control*, **53** (2006) 1895.

[23] Schröder C. and Scott W., *IEEE Trans. Geosci. Remote Sens.*, **38** (2000) 1505.

[24] Bottledooren D., *J. Acoust. Soc. Am.*, **102** (1997) 170.

[25] Anderson J., *Computational Fluid Dynamics: The Basics with Application* (McGraw-Hill) 1995.

[26] Secomb T., *J. Fluid Mech.*, **88** (1978) 273.

[27] Vainshtein P., Fichman M., Shuster K. and Gutfinger C., *J. Fluid Mech.*, **306** (1996) 31.

[28] Spengler J., Coakley W. and Christensen K., *AIChE J.*, **49** (2003) 2773.

[29] Tan M., Friend J. and Yeo L., *Appl. Phys. Lett.*, **91** (2007) 224101.

[30] Girardo S., Cecchini M., Beltram F., Cingolani R. and Pisignano D., *Lab Chip*, **8** (2008) 1557.